CrossMark

Structural, magnetic and electrical properties of Bi doped LaFeO$_3$ nano-crystals, synthesized by auto-combustion method

M. A. Ahmed[1] · A. A. Azab[2] · E. H. El-Khawas[3]

Abstract La$_{1-x}$Bi$_x$FeO$_3$; $0 \leq x \leq 0.2$ have been prepared by citrate auto-combustion method. The results of X-ray diffraction showed that LaFeO$_3$ has single phase with orthorhombic structure. With increasing Bi content, traces of secondary phase of rhombohedral structure are observed. The transmission electron microscope showed that the prepared compositions have nanocrystalline structure with an increase of the particle size increases with increasing Bi content. The magnetic properties of the samples were investigated by vibrating sample magnetometer, in which saturation magnetization (M$_s$) and coercivity (H$_c$) were determined. The value of Ms increases with increasing Bi content up to $x = 0.10$, while H$_c$ decreases with increasing Bi content. The temperature dependence of dielectric constant, dielectric loss and ac conductivity at different frequencies (100 kHz–5 MHz) were studied.

1 Introduction

Many branches of the modern chemical industry (e.g., catalysts chemical sensors, magnetic materials, electrode materials, and fuel cells) are dealing with the perovskite oxides ABO$_3$. A-site contains rare earth metal with large ionic radius and B-site has transition metal with smaller ionic radius in the range of (0.6–0.8 Å) [1–7]. In addition, the small cations (B) lies at the centre of an octahedron [BO$_6$] while the large cations (A) are inserted at the unit cell corners [8, 9]. These materials exhibit interesting magnetic and spin reorientation properties [4, 5, 10]. At room temperature LaFeO$_3$ crystallize is orthorhombic structure and exhibits a phase transition to the rhombohedral modification at temperature about of 987 °C [11]. The magnetic behavior of LaFeO$_3$ has two interpenetrating pseudo-cubic face-centered sub-lattices, which consist of FeO$_6$ octahedral units. This indicates the collinear arrangement of the two sub-lattices, giving an antiferromagnetic character. Das et al. [12] and Zhang et al. [13] suggested that La^{3+} substitution with Bi^{3+} eliminate impurity phases and destroy the cycloidal spin structure resulting in uniform canted antiferromagnetic ordering. Crystallite diameters, morphologies, and crystallinity of LaFeO$_3$ were highly influenced by the synthesis method. The synthesis of LaFeO$_3$ has been achieved using many methods, including solid-state reaction [14], sol–gel [15], co-precipitation [16], auto combustion [17], hydrothermal [18] and sonochemical [19]. In this work, the objective is to improve the magnetic properties of LFO-based materials. For this purpose, the La$_{1-x}$Bi$_x$FeO$_3$; $0 \leq x \leq 0.2$ compositions are prepared by auto-combustion method. The structure, morphology, magnetic and electrical properties of LFO crystallites are investigated for different Bi contents.

2 Experimental techniques

Orthoferrites with formula, (La$_{1-x}$Bi$_x$FeO$_3$); $0 \leq x \leq 0.20$ were synthesized using citrate – nitrate auto-combustion method [20]. Ferric nitrate (Fe (NO$_3$)$_3$.9H$_2$O), lanthanum

✉ A. A. Azab
aliazab@Hotmail.com

1 Materials Science Lab (1), Physics Department, Faculty of Science, Cairo University, Giza, Egypt

2 Solid State Electronics Laboratory, Solid State Physics Department, Physics Division, National Research Centre, 33 El Bohouth St., Dokki, Giza 12622, Egypt

3 Basic Science Department, Higher Technological Institute, Tenth of Ramadan City, Egypt

nitrate ($La(NO_3)_3.6H_2O$), bismuth nitrate ($Bi(NO_3)_3.5H_2O$) and citric acid were mixed stoichiometrically to get clear solution. The ratio of metal nitrates to citric acid was 1:1. Ammonia solution was added drop wise until the pH became 7. The mixture was stirred at 600 rpm and slowly evaporated at 130 °C to form gels. Viscosity and color were changed as sol turned into a brown puffy porous dry gel. The dried gel then ignited, undergoing a strong auto combustion process with evolution of large amount of gases. The as-synthesized product was calcined at 550 °C for 1 h with rate 4 °C/min to obtain orthoferrite powder.

X-ray diffractometer (Proker D8-USA) with Cukα radiation was employed to identify the crystal structure of the samples at room temperature. High resolution transmission electron microscope (JEOL JEM 2100) was used to examine the particle size and morphology. The magnetic measurements were carried out using a vibrating sample magnetometer (Lake Shore-7410) in applied magnetic field of 20 kOe and at room temperature. For electrical measurements, the powders were pressed into pellets using uniaxial press of pressure 1.9×10^8 Nm^{-2}. The samples were good polished to obtain uniform parallel surfaces. Contacts on the sample surfaces were made by silver paste and checked for good conduction. The real part of dielectric constant (ε') and the ac conductivity (σ_{ac}) were measured using the two probe method using LCR meter model Hioki type 3532 (Japan) as a function of temperature from 300 to 750 K at different frequencies ranging from 100 kHz to 5 MHz. The temperature of the samples was measured using a K-type thermocouple connected to a digit-sense thermometer with junction in contact with the sample.

3 Results and discussion

3.1 Microstructure analysis

Figure 1 shows the XRD patterns of $La_{1−x}Bi_xFeO_3$; $0 \leq x \leq 0.20$. From the first view, all peaks of the samples reveal single phase orthorhombic structure with space group (Pbnm) as indexed with ICCD card No. 74-2203. The crystallite size of the samples was determined according to the X-ray line-broadening of the (200) diffraction peak using the Scherrer's equation: $D = 0.89 \lambda/\beta \cos\theta$ [20, 21], where D is the crystallite size; λ is the X-ray wavelength (0.15406 nm for Cukα); β is the

Table 1 Values for the lattice parameters (a, b, c) and X-ray crystallite size (nm) of $La_{1−x}Bi_xFeO_3$; $0 \leq x \leq 0.2$

x	a (Å)	b (Å)	c (Å)	X-ray crystallite size (nm)
0.0	5.557	5.553	7.859	31.9
0.05	5.559	5.556	7.865	39.3
0.10	5.564	5.561	7.872	31.9
0.15	5.561	5.559	7.864	50.7
0.20	5.559	5.558	7.865	39

Fig. 1 X-ray diffraction patterns of $La_{1−x}Bi_xFeO_3$; $0 \leq x \leq 0.2$
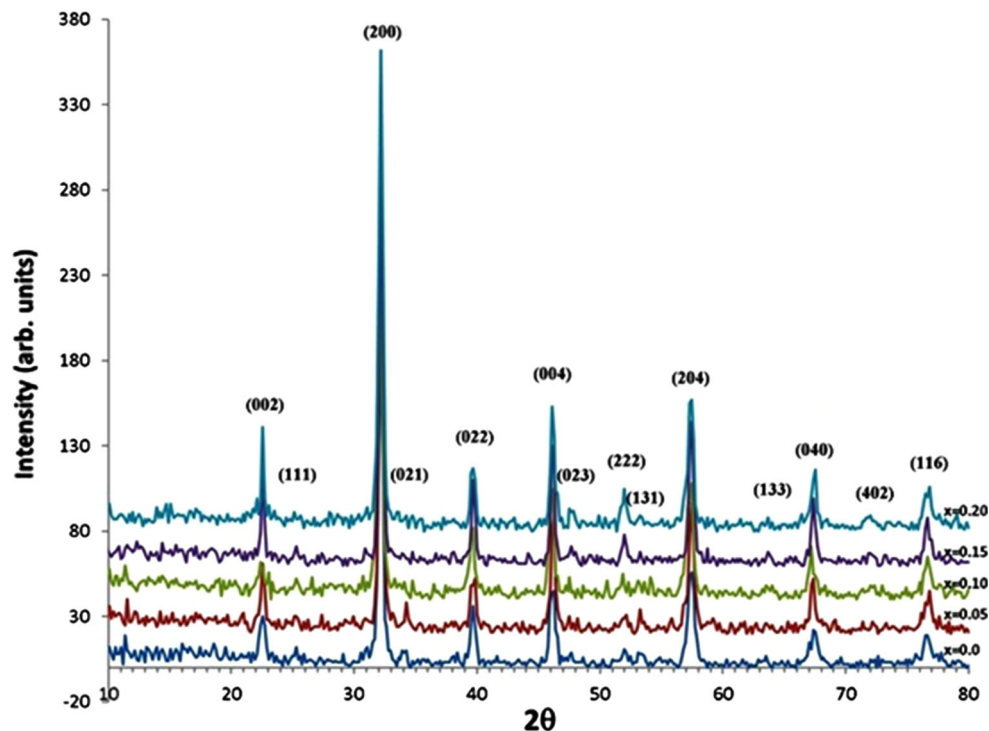
corrected FWHM of the diffraction peak. The average crystallite size was changed from 31.9 to 50.7 nm for the powders as reported in Table 1. The lattice parameters of the samples were calculated and reported in Table 1. Besides, the unit cell volume calculated from lattice parameters versus Bi content is shown in Fig. 2a. The unit cell volume increases with Bi content up to x = 0.10 which in agreement with the replacement of La^{3+} ion (1.16 Å) by Bi^{3+} ion (1.17 Å) [22] after that it decreases with further increase in Bi content. This decrease could be probably due to a structural phase transition in the Bi rich samples. An evidence of this suggestion is the splitting of the planes (116) and (023). The splitting becomes obvious as the Bi content increased. Recent research work [23] on $BiFeO_3$ reported the structural phase contains its orthorhombic by doping with rare earth elements on Bi site. Therefore one expected that same situation took place as Bi^{3+} replaces La^{3+} on orthorhombic structure. That is to distort the orthorhombic lattice into a rhombohedral hexagonal at high concentrations. A plausible explanation of the a decrease of all lattice parameters as well as the unit cell volume at x > 0.10 is that, the La^{3+} exist in ninefold coordination of the parent compound namely $LaFeO_3$ [24]. Doping $LaFeO_3$ with Bi^{3+} could lead to lowering the A cation coordination number leading to a situation in which La^{3+} ionic radius is 1.16 Å while that of Bi is 1.17 Å on eightfold coordination. This in turns will be reflected as a decrease in the Fe–O octahedron titling, therefore on expected increase in the tolerance factor as well as a change in the crystal symmetry with more Bi doping.

Figure 2b, gives an increase of X-ray density (D_x) with Bi content due to the increase in the molecular weight (Bi: 208.98, La: 138.91) which can't be compensated by the decrease in the unit cell volume after x = 0.10. The stability and distortion of the perovskite compounds are predicted by the so-called tolerance factor. The ideal perovskite is cubic structure with the tolerance factor of 1, as calculated from the relation [25, 26]

$$t = \frac{(r_A + r_O)}{\sqrt{2}(r_B + r_O)}$$

where r_A is the ionic radius of A cation, r_B is the ionic radius of B cation and r_o is the ionic radius of oxygen ion. The perovskite structure is stable in the range 0.75 < t < 1.0, and is cubic in the range t > 0.95 [27]. Figure 2c shows the increase of tolerance factor with Bi concentration due to the larger ionic radius of Bi^{3+}, which means that the orthorhombic distortion decreases with Bi content. Figure 3 represents the HRTEM micrographs of the samples with x = 0.0, 0.05 and 0.15. Nano-size particles with nearly spherical shape are observed in the samples. The particle size of the samples is ranges from 26 to
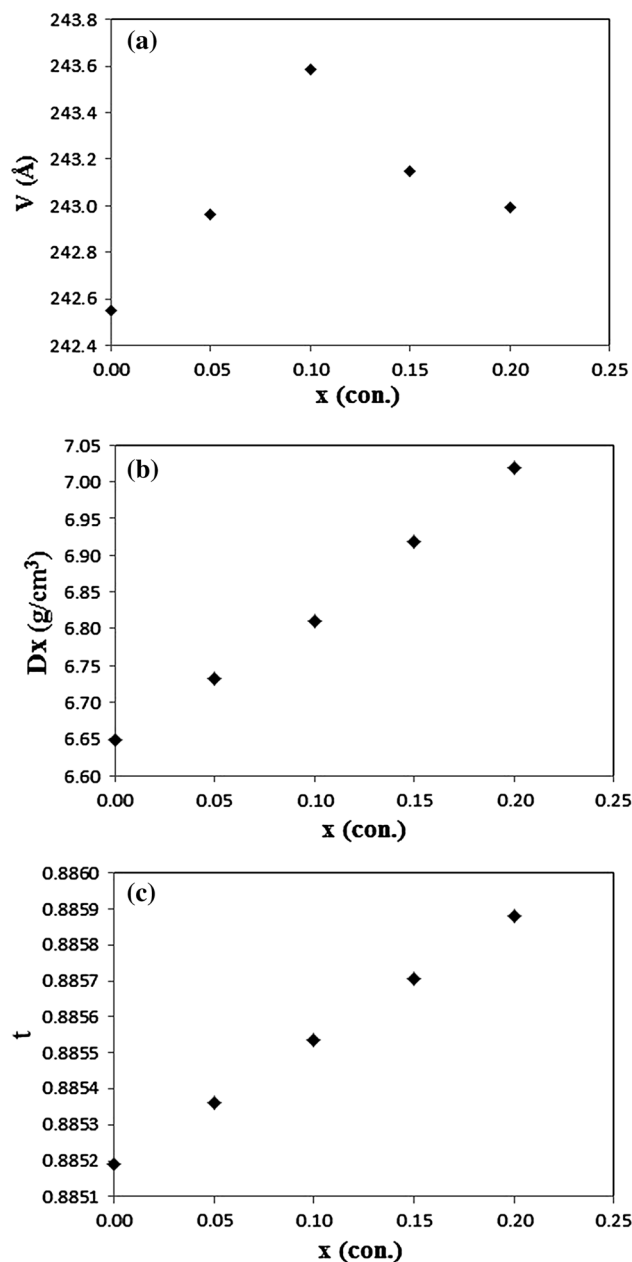

Fig. 2 **a** Unit cell volume (V), **b** X-ray density (D_x) and **c** tolerance factor (t) as a function Bi content of $La_{1-x}Bi_xFeO_3$; $0 \leq x \leq 0.2$

64 nm. It can be seen that the particle size of the prepared powders obtained from the HRTEM micrographs is slightly larger than that obtained from the XRD calculations. This result arises from the agglomeration of the particles due to the high surface energy of nanoparticles [28–31]. Besides, it can be stated that the average crystallite size determined by the XRD analysis tends to be lower than that observed in TEM [28]. HRTEM micrographs presented in Fig. 3b, shows that the nanoparticles exhibit clearly resolved lattice fringes with the interplanar spacing of 0.13 nm assigned to the (040) plane of the orthorhombic $LaFeO_3$ structure,
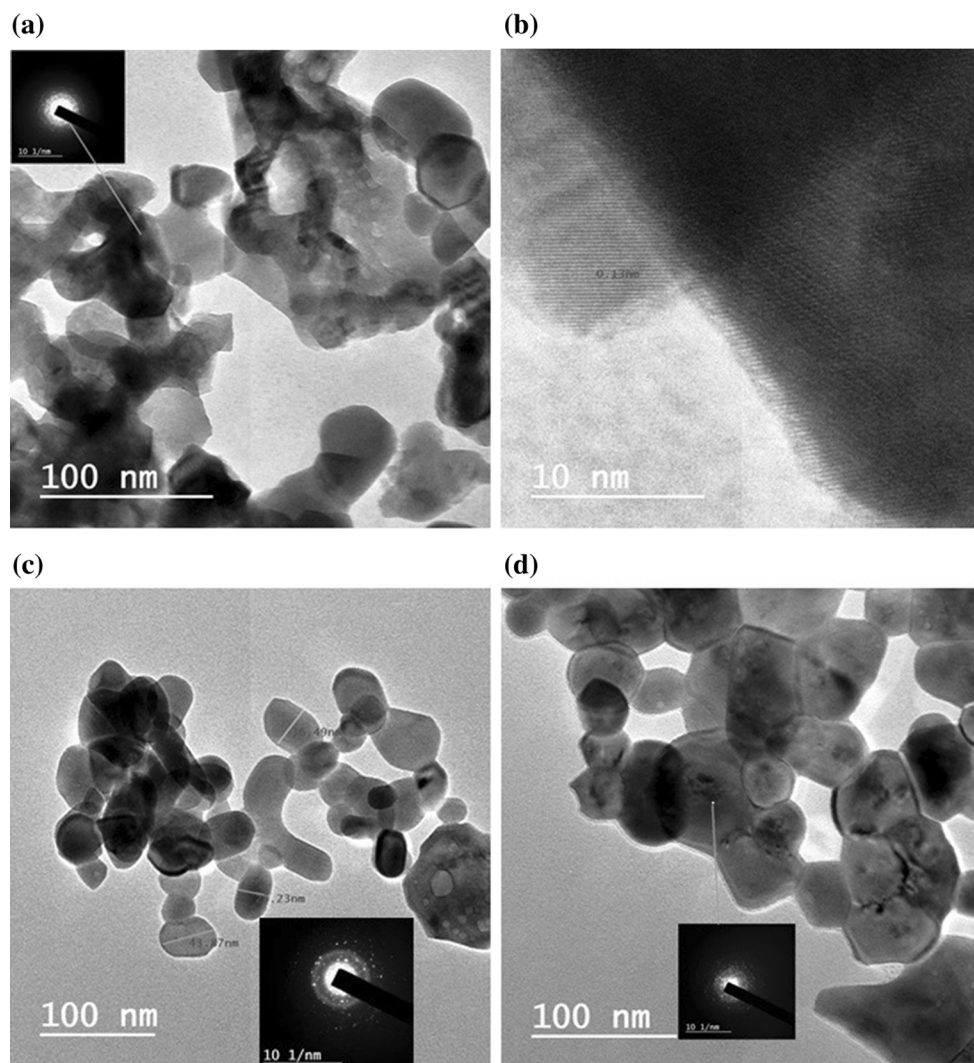
(a)

(b)

(c)

(d)

Fig. 3 HRTEM images and electron diffraction patterns of $La_{1-x}Bi_xFeO_3$; $0 \leq x \leq 0.2$. **a** x = 0, **b** x = 0, **c** x = 0.05, **d** x = 0.15

indicating the formation of high quality orthorhombic $LaFeO_3$ nanocrystals.

3.2 Magnetic properties

The crystalline structure of orthoferrites $LaFeO_3$ can be considerably deformed from the ideal perovskite structure. The magnetic symmetry of this configuration is (G-type) [31–33]. The magnetic super-exchange interactions between the Fe ions result in collinear antiferromagnetic AFM spin order which contributes to the AFM coupling along a particular crystallographic direction. However, low symmetry of the distorted orthorhombic perovskite-type structure leads to the tilt of FeO_6 octahedra. Consequently, a canted spin order is also formed in the Fe

lattice, which gives rise to weak ferromagnetic (WFM) along another crystallographic direction [34–37]. Therefore, both AFM and WFM ordering can be observed in the system influenced by the particle size and morphology. From Fig. 4 the samples show WFM properties for all samples. Qi et al. [35] have been observed that the AFM interaction is dominant in $LaFeO_3$ nanocrystallites prepared by the sol–gel auto-combustion method. It is also noted that drastic change in the shape of hysteresis loop and value of saturation magnetization (Ms) at x > 0. Figure 5a shows that, the value of M_s Increases with increasing Bi content up to x = 0.10 and then decreases. This behavior congruent with that observed in Fig. 2a in plotted the unit cell volume which increases also up to x = 0.10 and then decreases. This arises from the increase

Fig. 4 M–H hysteresis loops of La$_{1-x}$Bi$_x$FeO$_3$; $0 \leq x \leq 0.2$
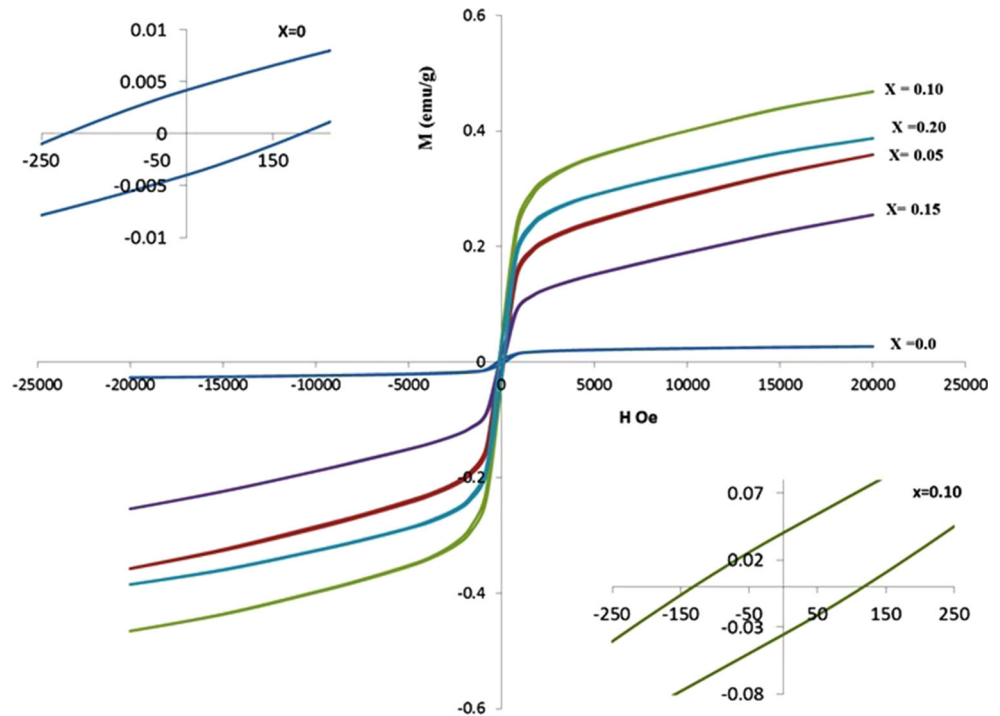
in unit cell volume which in turns increases the canting angle as well as the distortion resulting in increasing saturation magnetization. Figure 5c shows the decrease in coercivity (Hc) with increasing Bi content. This behavior in Hc is attributed to the decrease in the magneto-crystalline anisotropy with increasing in particle size. Qi et al. [35] reported a coercive field of LaFeO$_3$ $\sim$ 90 Oe and a saturation magnetization Ms $\sim$ 2.75 emu/g at room temperature and Shen et al. [36] reported a coercive field of LaFeO$_3$ 137 Oe and a spontaneous magnetization about 0.10 emu/g, while Sivakumar et al. [19] reported values of LaFeO$_3$ $\sim$ 250 Oe and $\sim$0.04 emu/g. Figure 5c shows the values exchange bias field, which depicted from the shift of the M–H loops (ΔHc) in the negative direction with respect to the origin. Wang and Ahmadvand [38, 39] reported on a loop shift that takes place for LaFeO$_3$ nanoparticles. The results were discussed in terms of an exchange coupling between a ferromagnetic-like shell and an antiferromagnetic core in nano-particles LaFeO$_3$ [40]. It is noted from Fig. 5c that the value of exchange bias field increases to its maximum value at x = 0.05 and then decreases with Bi content. This behavior can be explained in terms of a decrease in exchange coupling between a ferromagnetic-like shell and an antiferromagnetic core in nano-particles.

3.3 Dielectric properties

Normally, multiferroic material are either magnetically or electrically polarized, this is a simultaneously character. It is precisely noted that the interaction between the transition metal, iron, and the rare earth element that plays an important role in this magneto-electrical material stands on the movement of the spin waves which causes a significant increase in the electric polarization [41, 42]. The interaction between the ions of the elements creates one of the strongest magneto-electrical effects observed in materials. Figure 6 shows the variation of the dielectric constant with absolute temperature and frequency at different Bi content for La$_{1-x}$Bi$_x$FeO$_3$, $0.0 \leq x \leq 0.20$. The dielectric constant is weakly temperature dependent up to critical temperature at which the dielectric constant starts to increase rapidly. The critical temperature is 620 K for x = 0 and increases with increasing Bi content attaining 700 K for x = 0.20. The behavior of dielectric constant is interpreted on the basis of Maxwell–Wagner (MW) polarization. MW polarization may arise as a result of different extrinsic effects, mostly due to the electrode–sample contact, where a barrier layer, with high capacitance in parallel with a large resistance, is formed or there are
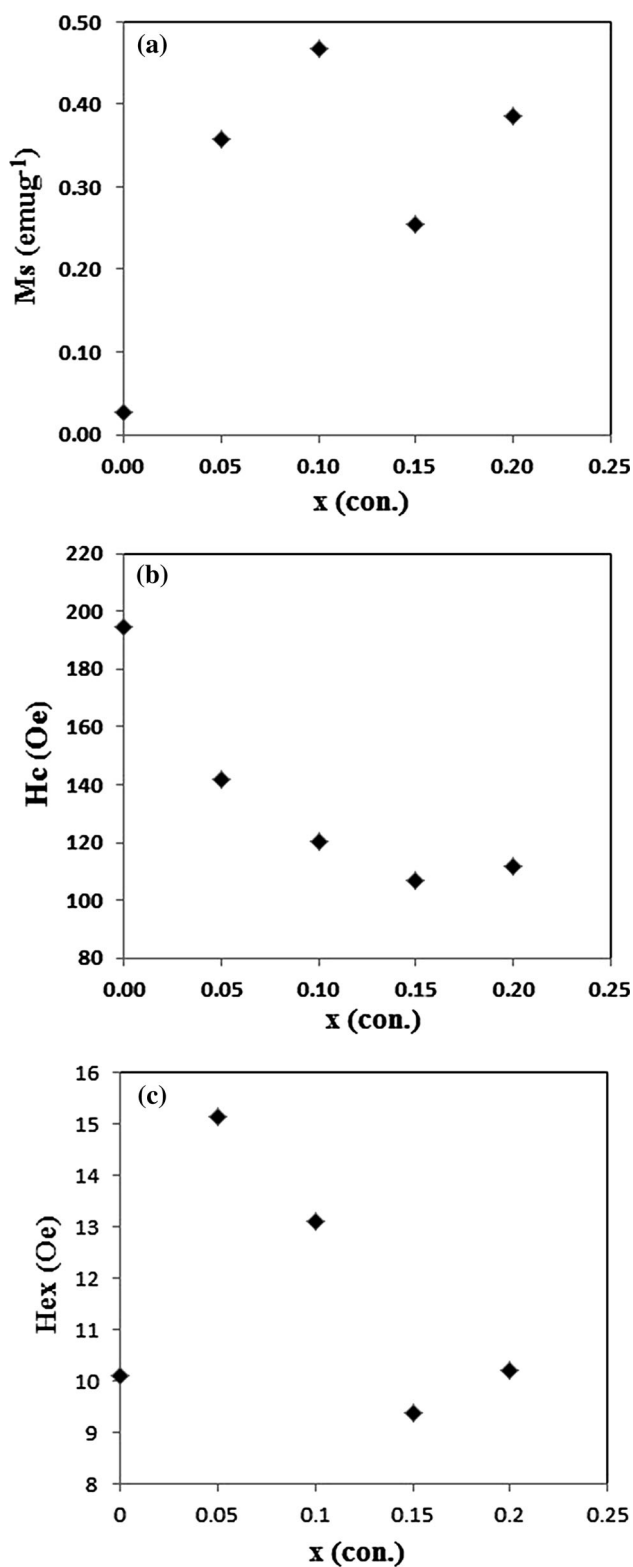
Fig. 5 Dependence of the magnetic properties on the Bi content of $La_{1-x}Bi_xFeO_3$; $0 \leq x \leq 0.2$. **a** Saturation magnetization Ms, **b** coercivity Hc, **c** exchange bias field

heterogeneities in the system, i.e., grain–grain contacts (grain boundaries) [43, 44]. At low temperatures, the electric dipoles cannot orient themselves with respect to the direction of the applied field and therefore contribute weakly to the polarization resulting in low value of ε'. As temperature increases most of the electric dipoles get enough thermal energy to be able to follow up the changes in the external field. This enhances the contribution of the dipoles to the polarization mechanism leading to an increase in the value of ε'. The large value of ε' at lower frequency is due to oxygen vacancies while the decrease in ε' at higher frequencies is expected because any species contributing to polarization is found to lag behind the applied field at progressively higher frequency. This phenomenon can be attributed to the Maxwell–Wagner-type and is related to the space charge relaxation at the interface. Figure 7 displays the imaginary part dielectric constant (ε'') with temperature at different frequencies (100 kHz–5 MHz). The observed peaks in ε'' for x = 0.05 and x = 0.20 can be attributed to existence of strong correlation between the conduction mechanism and the dielectric behavior as reported in ferrites [45, 46]. Accordingly, a peak is expected when the hopping frequency of the electrons, hopping between Fe^{2+} and Fe^{3+} ions is approximately equal to that of the external applied field, and in this case $\omega\tau = 1$ is valid, where t is relaxation time of the hopping process and ω is the angular frequency of the external applied field ($\omega = 2\pi\nu_{max}$) [47]. Figure 8 illustrates the dependence of ac conductivity on absolute temperature at different frequencies (100 kHz–5 MHz). The conductivity increases slightly with increasing temperature up to critical temperature. Above this temperature, the conductivity shows strong temperature dependence. The transition temperature from weak to strong dependence of conductivity on temperature depends on the Bi content which is consistent with that explained in dielectric data. The increase in conductivity with temperature may be due to enhancement of the mobility of charge carriers and the contribution of ionic conduction at relatively high temperature. The conductivity increases also with increasing frequency indicating that the frequency enhances the hopping of the charge carriers between Fe^{2+} and Fe^{3+} which is the principle of ac conduction in ferrites. Figure 9 represents the composition dependence of dielectric constant and ac conductivity at different frequencies and temperature 733 K. It is noted that both dielectric constant and ac conductivity decrease rapidly with increasing Bi content up to x = 0.10 and then they start to increase. This behavior can be correlated with

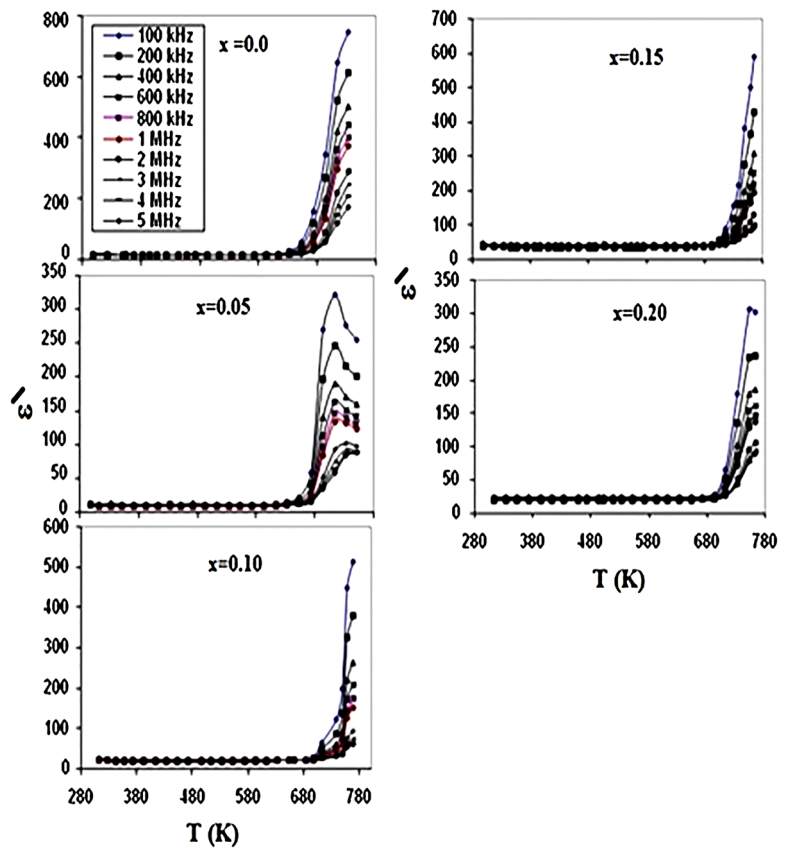**Fig. 6** Dielectric constant versus absolute temperature at different frequencies of La$_{1-x}$Bi$_x$FeO$_3$; $0 \leq x \leq 0.2$

Fig. 7 Imaginary part dielectric constant versus absolute temperature at different frequencies of La$_{1-x}$Bi$_x$FeO$_3$; $0 \leq x \leq 0.2$

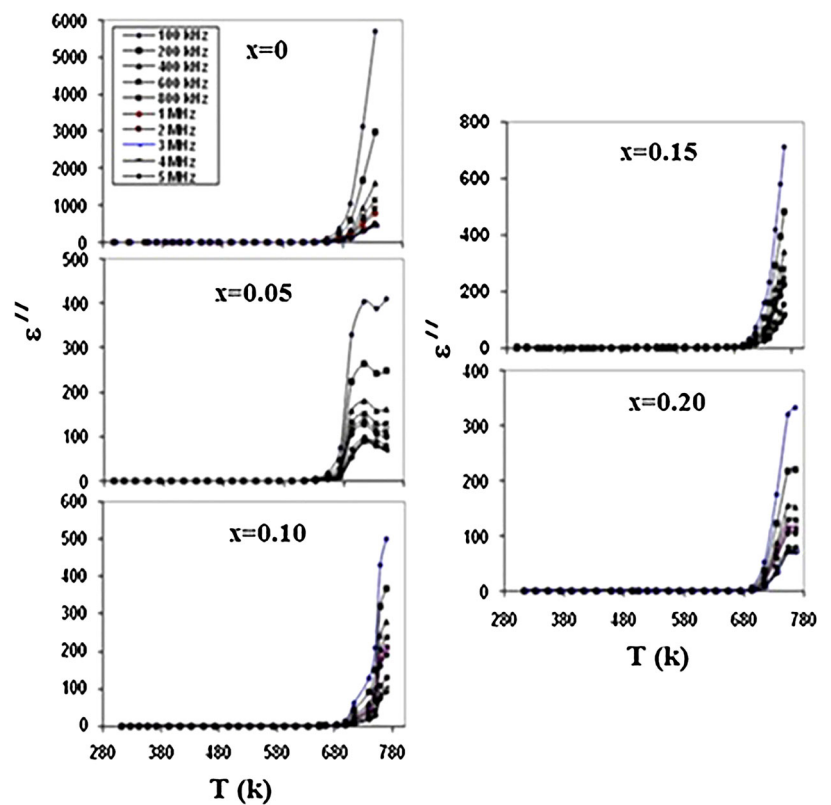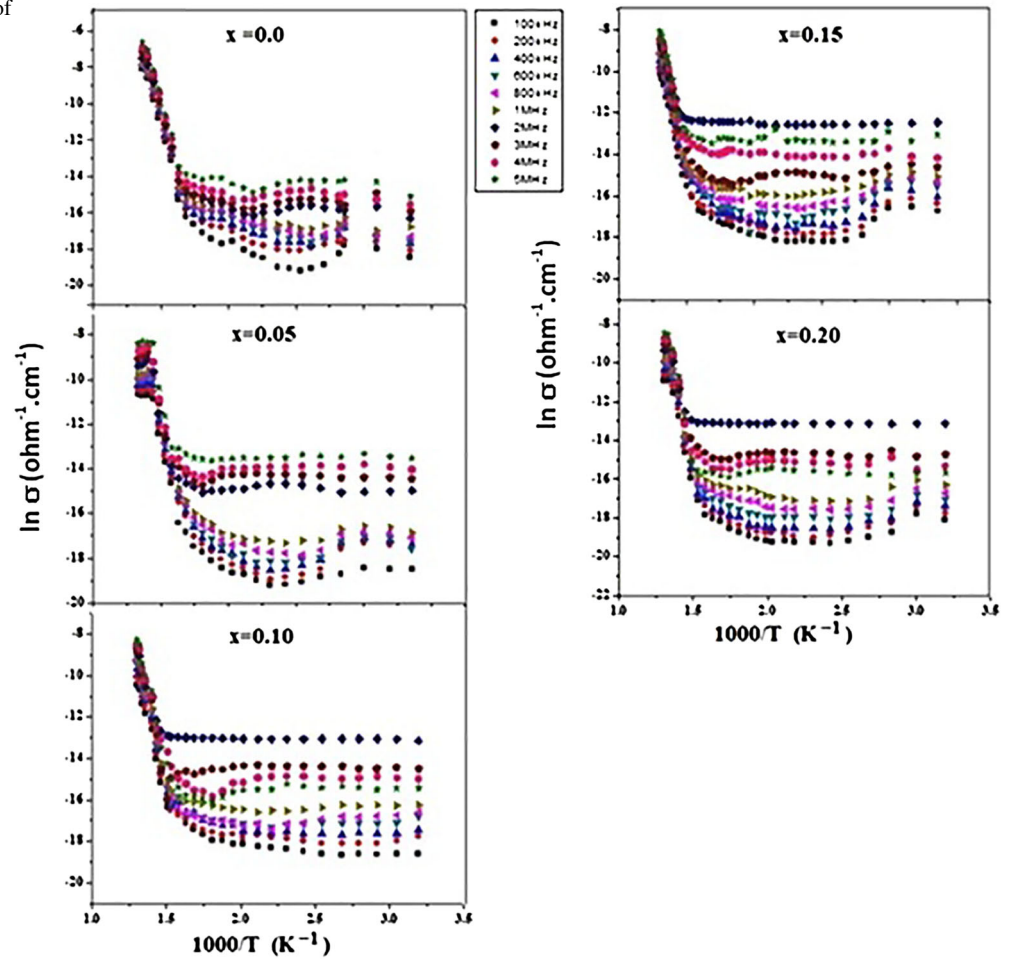**Fig. 8** Temperature dependence of ac conductivity as a function of frequency of $La_{1-x}Bi_xFeO_3$; $0 \leq x \leq 0.2$

behavior of unit cell volume against composition as shown previously in Fig. 2a. With increasing the unit cell volume, the distance of hopping between different valences ions increases resulting in decrease in ac conductivity. Likewise, for $x > 0.10$, the increase in conductivity and dielectric constant is attributed to the decrease in unit cell volume.

4 Conclusion

A series of $La_{1-x}Bi_xFeO_3$; $0 \leq x \leq 0.2$ has been prepared by auto-combustion method. X-ray diffraction showed single phase perovskite structures with space group (Pbnm), with doping Bi content rhombohedral structure started to appear as a secondary phase. The lattice parameters (a, b, c) of the samples increase with increasing Bi content up to $x = 0.10$ and then decrease with further increasing Bi. High-resolution transmission electron microscopy images reveal that the nano-structure of $La_{1-x}Bi_xFeO_3$, in which the crystallite size increases with increasing Bi content. The magnetization versus magnetic field at room temperature showed weak ferromagnetism influenced by both particle size and morphology. The dielectric constant and ac conductivity decrease with increasing Bi content up to $x = 0.10$ and then increase. It is concluded that the concentration $x = 0.10$ is a special one of its characters and relations with the above parameters and phenomena.
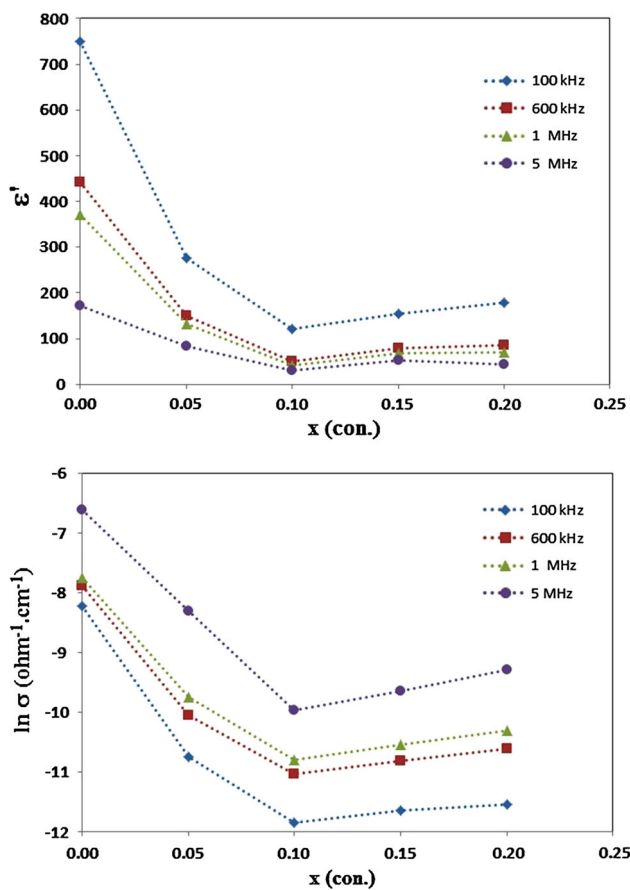
Fig. 9 Variation of dielectric constant and ac conductivity at 733 K and different frequencies as a function of the Bi content of $La_{1-x}Bi_xFeO_3$; $0 \leq x \leq 0.2$

References

1. S. Phokhaa, S. Hunpratupb, S. Pinitsoontornb, B. Putasaengc, S. Rujirawata, S. Maensiri, Mater. Res. Bull. **67**, 118–125 (2015)
2. Irshad Bhat, Shahid Husain, Wasi Khan, S.I. Patil. Mater. Res. Bull. **48**, 4506–4512 (2013)
3. A. Benali, S. Azizi, M. Bejar, E. Dhahri, M.F.P. Graça, Ceram. Int. **40**, 14367–14373 (2014)
4. M.B. Bellakki, C. Madhu, T. Greindl, S. Kohli, P. McCurdy, V. Manivannan, Rare Met. **29**, 491–500 (2010)
5. D. Hammer, J. Wu, C. Leighton, Phys. Rev. B **69**, 134407–134411 (2004)
6. E. Traversa, S. Matsushima, G. Okada, Y. Sadaoka, Y. Sakai, K. Watanabe, Sens. Actuators B **25**, 661–664 (1995)
7. M.A. Pena, J.L.G. Fierro, Chem. Rev. **101**, 1981–2017 (2001)
8. J.M. Liu, Q.C. Li, X.S. Gao, Y. Yang, X.H. Zhou, X.Y. Chen et al., Phys. Rev. B **66**, 054416–054427 (2002)
9. N.A. Hill, J. Phys, Chem. B **104**, 6694–6709 (2000)
10. M. Cherry, M.S. Islam, C.R.A. Catlow, J. Solid State Chem. **118**, 125–132 (1995)
11. S. Geller, P.M. Raccah, Phys. Rev. B **2**, 1167–1172 (1970)
12. S.R. Das, R.N.P. Choudhary, P. Bhattacharya, R.S. Katiyar, P. Dutta, A. Manivannan, M.S. Seehra, J. Appl. Phys. **101**, 034104 (2007)
13. S.T. Zhang, Y. Zhang, M.H. Lu, C.L. Du, Y.F. Chen, Z.G. Liu, Y.Y. Zhu, N.B. Ming, Appl. Phys. Lett. **88**, 162901 (2006)
14. L.T. Sagdahl, M.A. Einarsrud, T. Grande, J. Am. Ceram. Soc. **83**, 2318 (2000)
15. X.P. Dai, Q. Wu, R.J. Li, C.C. Yu, Z.P. Hao, J. Phys. Chem. B **110**, 25856–25862 (2006)
16. S. Nakayama, J. Mater. Sci. **36**, 5643–5648 (2001)
17. X.W. Qi, J. Zhou, Z.X. Yue, Z.L. Gui, Ceram. Int. **29**, 347–349 (2003)
18. W.J. Zheng, R.H. Liu, D.K. Peng, G.Y. Meng, Mater. Lett. **43**(1), 19–22 (2000)
19. M. Sivakumar, A. Gedanken, W. Zhong, Y.H. Jiang, Y.W. Du, I. Brukental, J. Mater. Chem. **14**, 764–769 (2004)
20. M.A. Ahmed, H.H. Afify, I.K. El Zawawi, A.A. Azab, J. Magn. Magn. Mater. **324**, 2199–2204 (2012)
21. A. Azab, E.H. El-Khawas, J. Appl. Sci. Res. **9**(3), 1683–1689 (2013)
22. R.D. Shannon, Acta Crystallogr. A **A32**, 751–767 (1976)
23. V.A. Khomchenko et al., J. Appl. Phys. **108**, 074109 (2010)
24. J.C. Yang et al., Phys. Rev. Lett. **109**, 247606 (2012)
25. C.F. Tseng, T.C. Wei, S.C. Lu, Ceram. Int. **40**, 7081–7085 (2014)
26. K. Ramam, K. Chandramouli, Ceram. Int. **37**, 979–984 (2011)
27. R.L. Cook, A.F. Sammells, Solid State Ion. **45**, 311–321 (1991)
28. F.Z. Qian, J.S. Jiang, S.Z. Guo, D.M. Jiang, W.G. Zhang, J. Appl. Phys. **106**, 084312 (2009)
29. Jun Wang, William B. White, James H. Adair, J. Phys. Chem. B **110**, 4679 (2006)
30. Thomas T. Morgan, Trevor M. Goff, James H. Adair, Nanoscale **3**, 2044–2053 (2011)
31. S.A. Ivanov, R. Tellgren, F. Porcher etn al. Mater. Res. Bull. **47**, 3253–3268 (2012)
32. R. Pushpa, D. Daniel, D.P. Butt, Solid State Ion. **249–250**, 184–190 (2013)
33. K. Mukhopadhyay, A.S. Mahapatra, P.K. Chakrabarti, J. Magn. Magn. Mater. **329**, 133–141 (2013)
34. A.A. Azab, N. Helmy, S. Albaaj, Mater. Res. Bull. **66**, 249–253 (2015)
35. X.W. Qi, J. Zhou, Z.X. Yue, Mater. Chem. Phys. **78**(1), 25–29 (2003)
36. H. Shen, G.F. Cheng, A.H. Wu, Phys. Status Solidi A **206**(7), 1420–1424 (2009)
37. P. Shikha, T.S. Kang, B.S. Randhawa, J. Alloys Compd. **625**, 336–345 (2015)
38. D. Wang, M. Gong, J. Appl. Phys. **109**, 114304 (2011)
39. H. Ahmadvand, H. Salamati, P. Kameli, A. Poddar, M. Acet, K. Zakeri, J. Phys. D Appl. Phys. **43**, 245002 (2010)
40. R.H. Kodama, S.A. Makhlouf, A.E. Berkowitz, Phys. Rev. Lett. **79**, 1393–1396 (1997)
41. P. Rovillain, R. de Sousa, Y. Gallais, A. Sacuto, M.A. Méasson, D. Colson, A. Forget, M. Bibes, A. Barthélémy, M. Cazayous, Nat. Mater. **9**, 975 (2010)
42. D.I. Khomskii, J. Magn. Magn. Mater. **306**, 1–6 (2006)
43. P. Lunkenheimer, V. Bobnar, A.V. Pronin, A.I. Ritus, A.A. Volkov, A. Loidl, Phys. Rev. B **66**, 052105 (2002)
44. J. Liu, C.G. Duan, W.G. Yin, W.N. Mei, R.W. Smith, J.R. Hardy, Phys. Rev. B **70**, 144106 (2004)
45. N. Rezlescu, E. Rezlescu, Solid State Commun. **14**, 69–72 (1974)
46. K. Iwauchi, Jpn. J. Appl. Phys. **10**, 1520–1528 (1971)
47. N. Nanba, J. Appl. Phys. **53**, 695–698 (1982)